PHYSICAL REVIEW E **89**, 032403 (2014)

Coexistence of spinodal instability and thermal nucleation in thin-film rupture: Insights from molecular levels

Trung Dac Nguyen,[1] Miguel Fuentes-Cabrera,[2,3] Jason D. Fowlkes,[2] and Philip D. Rack[3,4,*]
[1]*National Center for Computational Sciences, Oak Ridge National Laboratory, Tennessee 37831*
[2]*Center for Nanophase and Materials Science, Computer Science and Mathematics Division, Oak Ridge National Laboratory, Tennessee 37831*
[3]*Center for Nanophase and Materials Science, Oak Ridge National Laboratory, Tennessee 37831*
[4]*Department of Materials Science and Engineering, University of Tennessee, Knoxville, Tennessee 37996*

(Received 19 December 2013; published 14 March 2014)

Despite extensive investigation using hydrodynamic models and experiments over the past decades, there remain open questions regarding the origin of the initial rupture of thin liquid films. One of the reasons that makes it difficult to identify the rupture origin is the coexistence of two dewetting mechanisms, namely, thermal nucleation and spinodal instability, as observed in many experimental studies. Using a coarse-grained model and large-scale molecular dynamics simulations, we are able to characterize the very early stage of dewetting in nanometer-thick liquid-metal films wetting a solid substrate. We observe the features characteristic of both spinodal instability and thermal nucleation in the spontaneously dewetting films and show that these two macroscopic mechanisms share a common origin at molecular levels.

DOI: 10.1103/PhysRevE.89.032403 PACS number(s): 68.15.+e, 68.03.Hj, 68.08.De

I. INTRODUCTION

The rupture mechanism of thin films has captured great interest over the past two decades as the stability and instability of nanometer-thick films has far-reaching implications in nanoscience and technology [1,2]. Although the theoretical framework for thin-film stability dates back to the 1960s [3–12], many open questions remain with regard to the rupture origin of liquid films deposited on a solid substrate [13–16], partly because of the simultaneous presence of multiple destabilizing forces. In previous studies, polymeric and metallic systems were preferably chosen because the primary driving force therein is the van der Waals dispersion [17–31] that leads to the generally applicable power-law dependence of the disjoining pressure upon film thickness at constant temperature. The dewetting mechanism was then characterized either by fitting the characteristic wavelength and rupture time as a function of the initial thickness [17–19] or by image processing of the resulting hole patterns [22,23]. Nevertheless, it is nontrivial to deduce the rupture origin from experimental dewetting patterns at later stages due to the coexistence of the features of spinodal instability and thermal nucleation in the unstable regime [24,25] and the almost unavoidable presence of heterogeneous nucleation due to impurities in the liquid and defects at the interfaces. Additionally, van der Waals dispersion is not the only factor that determines the disjoining pressure. Density gradient [32], temperature gradient [33,34], thermoacoustic fluctuations [35–37], thermal noises [38–40], and molecular orientation fluctuations [41] can have nonnegligible influences on the effective disjoining pressure between the liquid-solid and liquid-vapor interfaces. Importantly, an appropriate functional form of the effective interfacial energy should be available to predict whether the film would be unstable at a given initial thickness.

Given the inherent challenges encountered by continuum models and experimental studies, molecular simulation provides a powerful tool for investigating the essential physics of the dewetting process. However, the length scale and time scale associated with unstable capillary waves are often many orders of magnitude greater than those of molecular scales. While many attempts to connect molecular dynamics simulations with continuum models have been made [42–52], a rigorous characterization of film rupture origin is still needed. Furthermore, while features of spinodal instability were suggested elsewhere [53,54], it was unclear if the hole formation might as well be due to nucleation, if there was a characteristic wavelength of the surface undulations associated with the rupture event, or if the rupture was dominated by nonequilibrium effects such as evaporation, temperature and density gradients, and external fields. For instance, Schebarchov *et al.* [54] indeed provided evidences that the film can only rupture when the substrate dimension is sufficiently large relative to the initial film thickness. The substrate size beyond which film rupture is observed was then attributed to the characteristic wavelength of unstable capillary modes. However, whether or not the growth in the amplitude of the most dominant surface undulation modes is associated with the formation of the first holes was not investigated.

In a recent study, we showed evidences that liquid-crystal thin films exhibit the characteristics of spinodal instability and thermal nucleation at liquid-vapor equilibrium, and that there would be a common origin for these two pathways at molecular levels, independent of initial thickness and liquid orientational ordering [55]. Based on the analysis framework proposed in that study, we investigate the early rupture stages of metallic thin films weakly wetting a solid substrate. Using a minimal model for liquid-liquid and liquid-substrate interactions and unprecedented large-scale simulations, we are able to characterize the features of spinodal instability and thermal nucleation as function of initial film thickness and temperature. Importantly, the hole formation process in all the studied films is shown to follow a consistent fashion, implying

---

[*] prack@utk.edu

a common underlying driving force at molecular levels. We then demonstrate that the driving force for film rupture is closely related to the energetic tendency of the liquid atoms to recover the local bulk-like environment. Notably, we find that the dewetting behavior of metallic films is highly similar to that of isotropic liquid-crystalline counterparts from microscopic perspectives despite their chemically distinct properties.

Our paper is organized as follows. Section II describes our simulation model and method. Simulation results and analysis are presented in Sec. III. We then discuss our findings in Sec. IV and conclude in Sec. V.

II. MODEL AND SIMULATION METHOD

The system we have modeled is a liquid-copper film on solid graphite. We focus on substrate-liquid-vacuum systems in which the liquid is nonvolatile, and liquid-liquid and solid-liquid interactions are apolar. Because the hydrodynamic properties of the liquid is important, we use the embedded atom model (EAM) potential [56,57] to model the liquid-liquid interaction. The EAM potential captures the many-body interaction between atoms, and is well known to yield liquid viscosity and surface tension consistent with experiment data. Specifically, we choose the EAM parameters for liquid copper so that our results can be qualitatively compared with previous studies [28,30,58]. This of course does not mean the model is restricted to the specified material.

As our first attempts, we choose the Lennard-Jones (LJ) 12-6 potential to model the interaction between liquid atoms and substrate atoms, acknowledging that the LJ potential is not the most accurate model for the solid-liquid surface tension. The LJ potential with the length scale of $\sigma = 0.3225$ nm is truncated and shifted to zero at the cutoff distance of $r_c = 2.5\sigma = 0.80625$ nm. The well depth of the LJ potential, ϵ, is set to be 0.01 eV, which gives an equilibrium contact angle of approximately 138° [58]. We do not use any correction for the long-range effect of the semi-infinite substrate because the solid-liquid interaction is assumed apolar and nonelectrostatic. The solid substrate consists of three layers arranged as in a graphitic structure with the layer spacing of $2.08\sigma = 0.67$ nm [58]. The substrate atoms are kept immobile throughout the course of simulation.

The procedure to conduct the dewetting computer experiments is given as follows. First, the liquid atoms are equilibrated in bulk at constant temperature for 300–500 ps. After equilibration, the liquid bulk is deposited on the substrate at the distance of $d = 2^{1/6}\sigma$, corresponding to the LJ well-depth location. The liquid atoms with the coordinate $z \geqslant z_u = d + h_0$ are then removed, leaving a film of initial thickness approximately h_0. A vacuum space of 20 nm in height is then added above the film-free surface. The initial vacuum gap is sufficient to avoid the effects of periodic boundary condition in the z direction for the early stage of dewetting, given the interaction cutoffs and the distance between substrate top and bottom layers.

The simulation proceeds with the liquid atoms equilibrated at constant temperature. An example of a simulated system with $h_0 = 0.8$ nm is illustrated in Fig. 1(a). Figure 1(b) shows the initial density profile of the film across its thickness for different values of h_0 at $T = 1800$ K. Using a small bin size of 0.01 nm reveals the oscillations in the liquid density across the film thickness [Fig. 1(b), inset]. The peak of the radial distribution function of the liquid atoms in bulk is located at approximately 0.25 nm, giving an estimate of the distance between a given liquid atom with its nearest neighbors. For $h_0 = 0.3$ nm, we observe that the amount of liquid atoms that becomes volatile increases remarkably as the liquid-vapor coexistence point is expected to shift toward lower temperatures for thinner films [47,49]. As a result, we only report the results for $h_0 \geqslant 0.4$ nm. The substrate dimension, L, is varied up to approximately 459 nm, to ascertain that the results are not biased by finite-size effects due to periodic boundary conditions in the x and y directions.

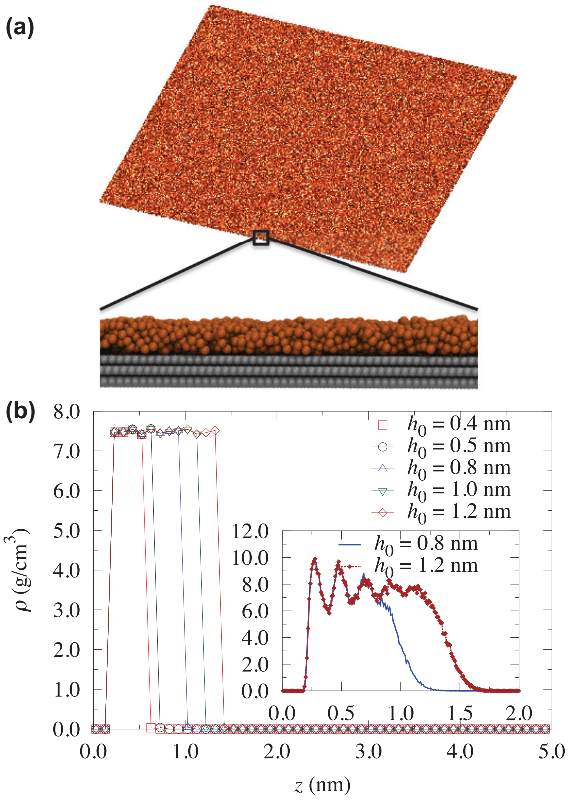

FIG. 1. (Color online) (a) Perspective view of a simulated system, of which $h_0 = 0.8$ nm and the substrate dimension $L = 459$ nm. The zoomed-in image shows the side view, liquid atoms are in orange color, substrate atoms in gray color. (b) Initial density profiles across the film thickness for different values of h_0 at $T = 1800$ K, the liquid density $\rho \approx 7.58$ g/cm^3. The bin size is 0.1 nm. Inset: Representative density profiles of the liquid atoms across the film thickness using the bin size of 0.01 nm.

To obtain the Fourier transforms of local thickness, we perform the following procedure. First, we partition the simulation box into N_b by N_b columns perpendicular to the substrate plane and bin the liquid atoms into the columns based on their coordinates at a given time step. Because evaporation is negligible over the whole course of simulation for $h_0 \geqslant 0.4$ nm for $T = 1500$–2200 K, the number of atoms in a bin, $n(x,y)$, is representative of the local film thickness: $h(x,y) = n(x,y)/[\rho^*(L/N_b)^2]$, where ρ^* is the liquid number density. Fourier transforms are then obtained for the N_b by N_b

matrix $h(x,y)$ at the given time step. The number of bins in each dimension is chosen as $N_b = 256$ or 512, which gives the average number of atoms per bin ranging from 10 to 40, depending on h_0, L, and N_b.

We identify "holes" as separate clusters of almost empty bins based on the normalized local thickness at a given time t: $h_*(x,y,t) = h(x,y,t)/h_{\max}(t)$, where $h_{\max}(t) = \max_{x,y}[h(x,y,t)]$. Almost empty bins are those with $h_* \leqslant h_c = 0.01$, which is sufficient to take into account holes containing few atoms. The critical thickness, h_c, is set so as to distinguish "holes" from "valleys," i.e., troughs on the free-liquid surface that do not touch the substrate. The time evolution of the number of holes, N_h, and their total area, A_h, are also used to monitor the rupture time scales. For all of the time evolutions reported, the time origin $t = 0$ is set at the time the film is deposited on the substrate. We define the rupture time, t_r, as the time when the hole total area starts to increase monotonously. The time to achieve the maximum number of holes is defined as t_m. The breakup duration is then defined as the interval from t_r until t_m: $\Delta t_b \equiv t_m - t_r$.

Molecular dynamics (MD) simulations are performed using LAMMPS [59] with the GPU accelerated version of the EAM and Lennard-Jones potentials [60,61]. The liquid temperature is maintained using the Nose-Hoover thermostat with a relaxation time of 0.1 ps to ensure that hydrodynamic interactions between liquid atoms are conserved [62] and that liquid surface tensions and viscosity are reasonably captured. The use of the Nose-Hoover thermostat for the liquid atoms certainly needs further justification so as to capture the nonequilibrium nature of the dewetting process. As first attempts to model metallic thin films melted by nanosecond laser pulses, we assume in the present study that the liquid temperature is invariant during the early stage of dewetting, which lasts within a few nanoseconds. The equations of motion of the liquid atoms are solved using the velocity Verlet algorithm with the time step of $\Delta t = 3.0$ fs. The simulations are performed using the Titan supercomputer at the Oak Ridge National Laboratory Leadership Computing Facility (OLCF).

III. RESULTS

We observe that films with $h_0 = 0.4$–1.5 nm spontaneously dewet within several nanoseconds; those with $h_0 \geqslant 1.8$ nm, however, do not dewet after tens of nanoseconds for substrate dimension L up to 459 nm. Depending on h_0 and L, we vary the number of liquid atoms from 500 000 to 40 000 000; the total number of atoms ranges from 1 000 000 to 90 000 000, including the substrate atoms. The number of compute nodes varies from 16 to 625 giving the number of atoms per node of 50 000–150 000.

A. Intermediate dewetting morphologies

Representative dewetting morphologies for different initial thicknesses at $T = 1800$ K and $\epsilon = 0.01$ eV are shown in Fig. 2. We notice that the $h_0 = 0.4$ nm film breaks into an interconnected morphology, reminiscent of spinodal decomposition in binary mixtures. This pattern was attributed to one of the pathways dictated by spinodal instability where liquid domains retract [7]. The dewetting pattern in $h_0 =$ 0.6 nm is characterized by a high hole number density, also consistent with the other instability pathway in which the holes expand rapidly [7]. Meanwhile, the dewetting pattern in the $h_0 = 0.8$-nm film appears to be similar to thermal nucleation induced dewetting [17]. For $h = 1.2$ nm, much fewer holes form in the absence of any surface undulation correlation, as described below. The dewetting behavior as a function of h_0 observed in our simulations is in excellent qualitative agreement with experimental studies [17,18,21,27,29].

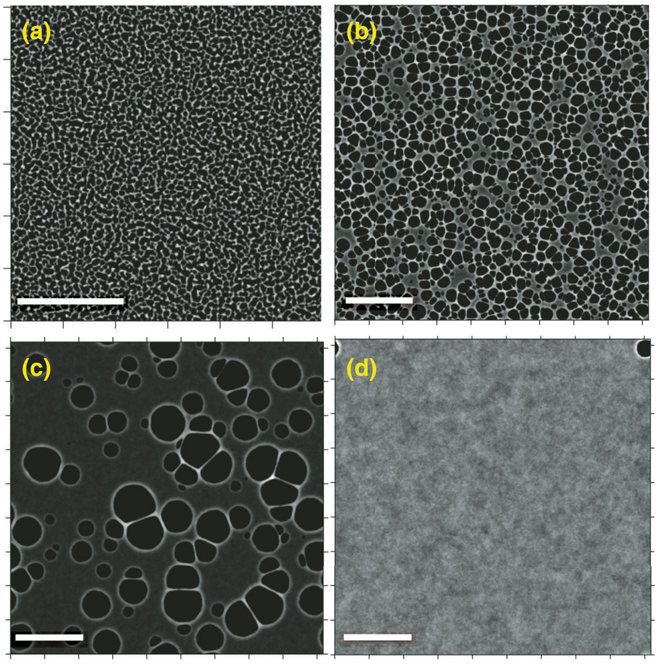

FIG. 2. (Color online) Representative intermediate dewetting morpholgies of (a) $h_0 = 0.4$ nm ($t = 12$ ps); (b) $h_0 = 0.6$ nm ($t = 30$ ps); (c) $h_0 = 0.8$ nm ($t = 90$ ps), and (d) $h_0 = 1.2$ nm ($t = 1.1$ ns). Local thickness values are in gray scale: the thicker regions are brighter. Scale bars correspond to 100 nm.

To investigate more closely the early stage of the dewetting process, we show in Fig. 3 the time evolutions for the films given in Fig. 2. For $h_0 = 0.4$ nm [Fig. 3(a)], a large number of holes form within a short time period ($t = 3$ ps), the liquid domains between the holes subsequently retract ($t = 6$ ps), and the interconnected morphology emerges after ∼10 ps. For $h_0 = 0.8$ nm, holes form scarcely and continuously over a certain period, on the order of picoseconds [Fig. 3(b)]. It is important to note that the Fourier transforms of the local thickness for $h_0 = 0.4$ and 0.8 nm indicate that the thickness variation is isotropic yet possesses a finite correlation length, which shifts to larger values, i.e., smaller q's, as the holes grow and coarsen. For $h_0 = 1.2$ nm, it takes approximately 1.0 ns to observe the first hole to form, remarkably longer than for the $h_0 = 0.8$ nm. Unlike the other thinner films, however, the surface undulation spectrum does not show any correlation at the low q limit, i.e., long-wave fluctuations, when the hole appears (Fig. 3(c), insets). We also perform the same Fourier analysis for the $h_0 = 2.0$-nm films, which do not dewet within our simulated time and length scales, and do not observe any characteristic wavelength in the long-wave regime at steady state.

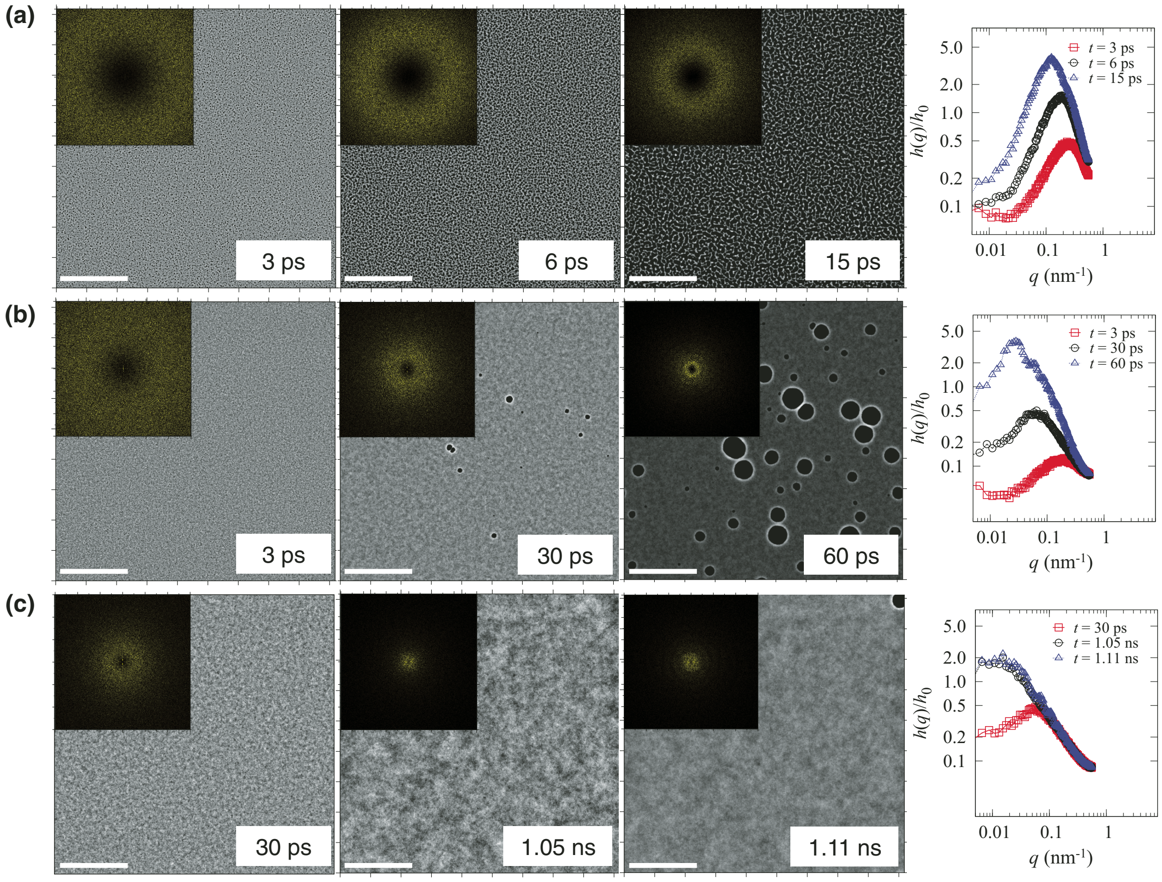

FIG. 3. (Color online) Time evolution of (a) $h_0 = 0.4$ nm; (b) $h_0 = 0.8$ nm, and (c) $h_0 = 1.2$ nm. Scale bars correspond to 100 nm. Insets are the corresponding Fourier spectra. The cutoff frequency of the 2D spectra is identical in all the insets, $q_{\max} = 0.3\ \text{nm}^{-1}$. The plots in the right column are the corresponding radially averaged spectra of the 2D insets. The substrate dimension is $L = 459$ nm in all cases plotted here.

B. Coexistence of spinodal instabilty and thermal nucleation features

As pointed out by experimental studies [15,24,25,63], spinodal instability and thermal nucleation are simultaneously active. Instead of trying to separate the two mechanisms from each other, we find the correlation between the distinct features of spinodal instability, i.e., characteristic wavelengths of surface undulation and rupture time, and the hole formation process. For this purpose, we focus our analysis on the stage before hole coarsening, $t < t_m$.

We first investigate the rupture time scales by monitoring the hole number density and area fraction during the dewetting process (Fig. 4). The hole number density, N_h/L^2, for all the studied films exhibits a consistent behavior: a delay before the rupture starts at t_r, followed by an early exponential increase, and a gradual slowing down until the maximum value is reached at t_m. After t_m, the hole number density decreases as the holes coalesce, as indicated by the monotonous increase in the hole area fraction, A_h/L^2 [Fig. 4(b)]. When we rescale the time evolution of the hole area fraction, A_h, in the precoarsening stage (i.e., $t < t_m$) with the time origin shifted to the rupture time, the data collapses nicely into a single curve [Fig. 4(c)]. The breakup duration, Δt_b, monotonously increases with h_0. During this interval, existing holes may collapse or grow, inducing or suppressing the formation of new holes nearby. We note that the area fraction provides a more reliable measure for the rupture time t_r than the hole number density does, because small holes appear and heal before rupture actually begins.

The dependencies of the time scales and hole number density on h_0 are shown in Fig. 5. To ensure that the results are not influenced by initial configurations nor by the finite-size effects associated with the periodic boundary conditions, we vary the substrate dimension from approximately 170 to 460 nm. It is important to emphasize that the data points fit nicely into respective power laws only when the substrate dimension exceeds certain values for the range of h_0 of interest. Specifically, the rupture time (t_r) and the time to achieve maximum hole number density (t_m) scale with $h_0^{4.8}$ and $h_0^{4.4}$, respectively, when using $L \geqslant 250$ nm for $h_0 \leqslant 1.0$ nm. Meanwhile, the maximum hole number density scales with $h_0^{-9.6}$. Using substrate dimensions as small as $L = 77$ nm and $L = 170$ nm yield longer rupture time scales and considerably fewer holes (yet a slightly higher hole number density) for $h_0 \geqslant 0.8$ nm. This suggests that statistics on the hole formation is poor in the thicker films using these values of L. It also appears that the ratio L/h_0 should be greater than 170 for convergence for the thin-film system under investigation.

Recall that continuum models (CM) where the van der Waals contribution to the disjoining pressure is proportional

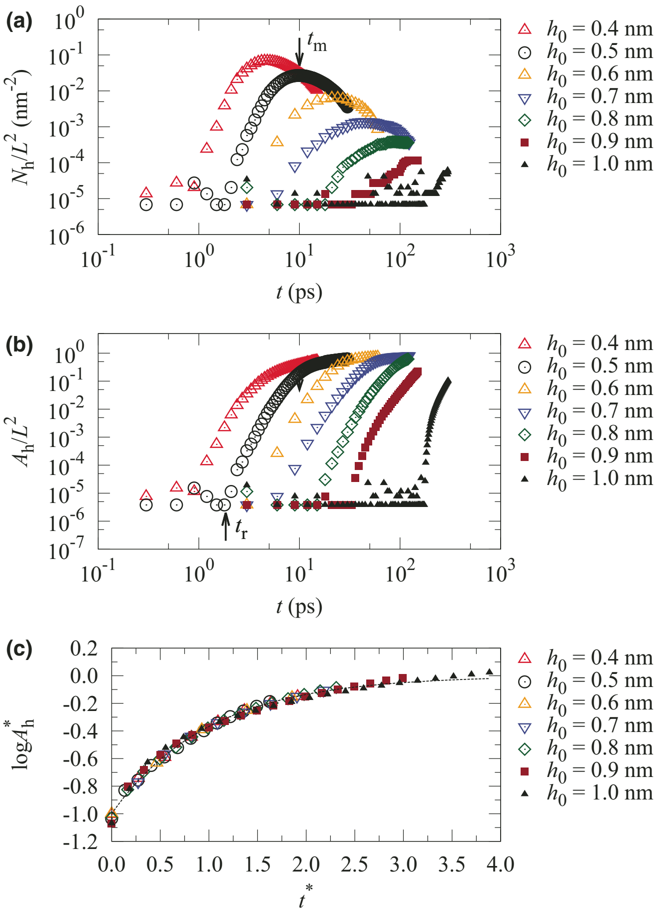

FIG. 4. (Color online) Time evolution of (a) number of holes per unit area, N_h/L^2, and (b) hole area fraction, A_h/L^2, for different values of h_0 plotted in the log-log axes. The arrows in (a) and (b) indicate the time to achieve the maximum hole number density (t_m) and the rupture time (t_r), determined for the $h_0 = 0.5$ nm film, as an example. (c) Time evolution of the dimensionless hole area fraction for all films studied. The dimensionless hole area fraction is defined as $\log A_h^* \sim \log(A_h/L^2)$ and the rescaled time as $t^* = (t - t_r)/\alpha$. $\log A_h^*$ is fitted with the saturation law $f(x) \sim 1 - \exp(-x/\alpha)$, where α is the relaxation time. The dotted line is drawn to guide the eyes. The substrate dimension is $L = 383$ nm for all cases plotted here. The relaxation time α obtained from the fitting are as follows: $h_0 = 0.4$ nm, $\alpha = 1.09$ ps; $h_0 = 0.5$ nm, $\alpha = 2.21$ ps; $h_0 = 0.6$ nm, $\alpha = 6.47$ ps; $h_0 = 0.7$ nm, $\alpha = 11.02$ ps; $h_0 = 0.8$ nm, $\alpha = 18.1$ ps; $h_0 = 0.9$ nm, $\alpha = 18.1$ ps; $h_0 = 1.0$ nm, $\alpha = 16.2$ ps.

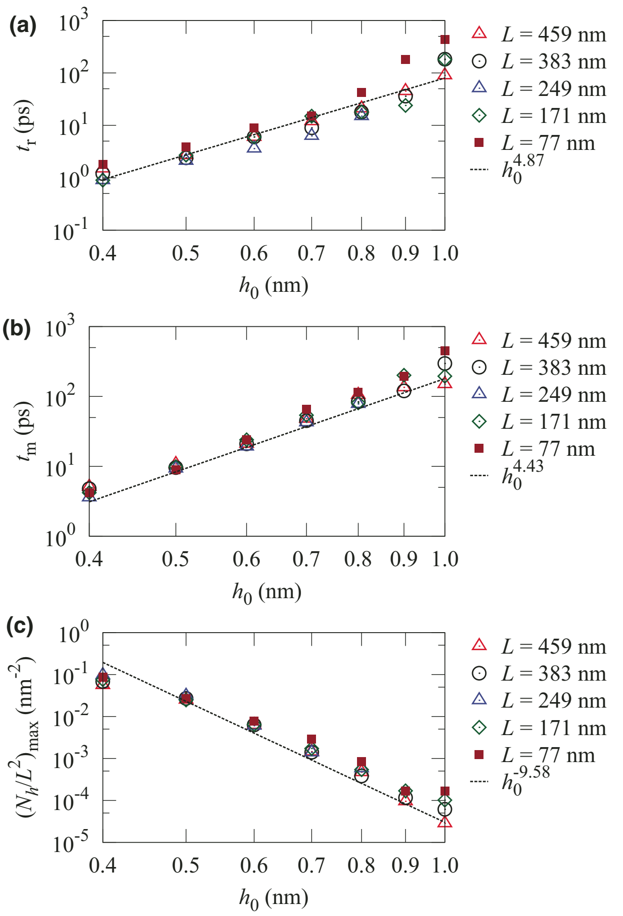

FIG. 5. (Color online) Dependence of (a) rupture time, (b) time to achieve maximum hole number density, and (c) maximum hole number density, $(N_h/L^2)_{\max}$ upon initial thickness h_0 for different values of substrate dimension L.

to $1/h^3$ predict that $(N_h/L^2)_{\max} \sim 1/\lambda_m^2 \sim h_0^{-4}$ and $\tau_m \sim h_0^5$, where λ_m and τ_m are the length and time scales of the fastest growing unstable modes [6,7,21]. While the time scales in our simulation results are in good qualitative agreement with CM, the length scale exhibits a more significantly rapid decay. We suppose that the particular CM might underestimate the roles of the fast hole growth during the rupture duration that suppress the formation of many potential holes. In other words, nonlinear effects associated with the growth of the early holes suppress the growth of linearly unstable modes.

For any arbitrary generic form of the effective interfacial potential, spinodal instability dictates that $(N_h/L^2)^2_{\max}\tau_m \sim h_0^{-3}$ [21]. According to the scaling powers previously obtained, our simulation data yields $(N_h/L^2)^2_{\max}\tau_m \sim h_0^{-14.0}$ using either t_m or t_r as the rupture time scale. The obvious deviation of our data from the linear stability analysis predictions indicates that thermal fluctuations at molecular scales, which are absent in the latter model, should play an influential role in the dewetting behavior. In a related work, MD simulations also suggested that stochastic fluctuations influenced the breakup of supported, sub-10-nm-diameter liquid-metal filaments where the Rayleigh-Plateau instability ultimately drives filament breakup [31]. This is reasonable for the thin films under investigation because the characteristic dimension of fluid flows, h_0, becomes comparable to the molecular mean free path, i.e., when the Knudsen number is close to unity [64].

Because thermal fluctuations within the film are dictated by temperature, it is expected that the rupture time scale and length scale are influenced by temperature. Indeed, we observe that t_m and $(N_h/L^2)_{\max}$ are strongly dependent upon temperature. As shown in Fig. 6, holes form more rapidly and at higher density upon increasing T for all values of h_0. It is also evident that as T is decreased toward the liquid-solid transition, which is approximately 1400 K for the EAM potential in use, the hole number density decreased remarkably. These trends suggest that the magnitude of thermal fluctuations *within* the

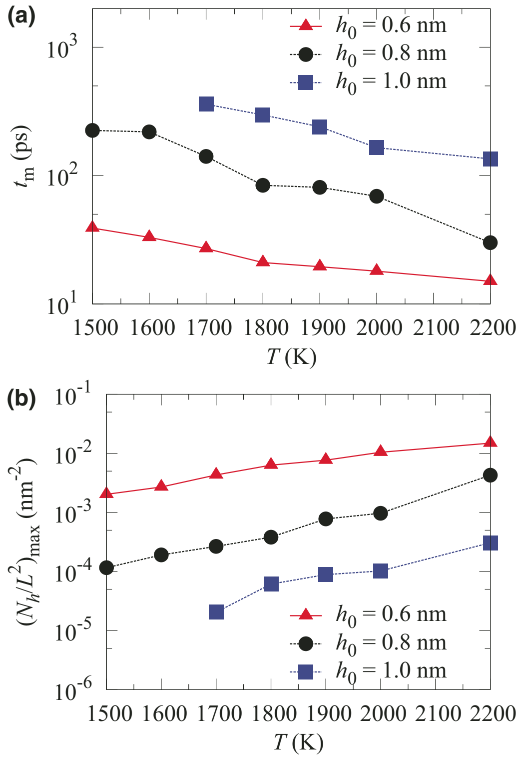

FIG. 6. (Color online) Temperature dependence of the time to achieve maximum hole number density, t_m, and the maximum hole number density, $(N_h/L^2)_{\max}$, for different values of h_0. The substrate dimension is $L = 383$ nm for all data points.

film plays an important role in the dewetting process. This is in line with previous studies using continuum models, where the net disjoining pressure incorporated thermoacoustic fluctuations in addition to van der Waals dispersion [35–37].

We proceed by computing the radially averaged Fourier spectra over the dewetting process based on the fact that the Fourier transforms are symmetric in all azimuthal angles. An example of the time evolution of the radially average Fourier spectra in the $h_0 = 0.7$ nm is given in Fig. 7(a). The peak of the spectra corresponds to the dominant wavelength of the surface undulations at the given time steps. According to Figs. 4(a) and 4(b), we can estimate $t_r = 6 \pm 3$ ps and $t_m = 45 \pm 3$ ps for $h_0 = 0.7$ nm. During the breakup duration, the peak is relatively unchanged at $q_m = 0.078$ nm^{-1}, corresponding to the characteristic wavelength of $\lambda_m = 12.7$ nm [Fig. 7(b)]. These are distinctive signatures of the characteristic length scales dictated by spinodal instability as given by continuum models [6,7].

To correlate the growth of the dominant surface undulation modes with the hole formation process, we monitor their magnitude, $h(q_m)$, relative to h_0. The undulation magnitude at q_m becomes comparable to h_0, indicating that the surface undulations caused by the dominant mode has reached the substrate. For instance, it takes approximately 27 ps for $h(q_m)/h_0 \approx 1$ in the $h_0 = 0.7$-nm film [Fig. 7(a)]. In this case, a considerable fraction of the holes already formed [see Fig. 4(a)] when the dominant surface undulation reaches the substrate. Therefore, the formation of the holes at the early stage of rupture is not related to the growth of the unstable modes of surface undulations. The presence of the holes preceding the growth of the fastest growing unstable modes implies the coexistence of spinodal instability and thermal nucleation features throughout the breakup duration.

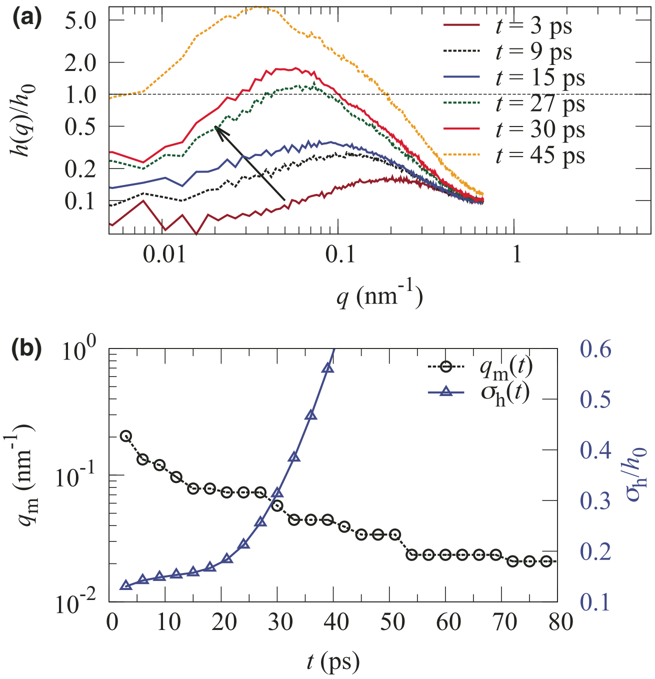

FIG. 7. (Color online) Time evolution of (a) radially averaged surface undulation spectra, (b) spectrum peak (q_m) and local thickness standard deviation (σ_h) for $h_0 = 0.7$ nm. The substrate dimension is $L = 383$ nm. The arrow in (a) indicates the direction of time progress.

Note that the standard deviation of local thickness σ_h is not representative of the growth of surface undulations: e.g., $\sigma_h < 0.3\,h_0$ even when the hole number density reached its maximum [Fig. 7(b)]. This is probably because the surface undulations during breakup duration deviate from Gaussian distributions. Also, the increase in $h(q_m)$ in the hole coarsening stage ($t > t_m$) is not related to the rupture mechanism.

The above analysis procedure is carried out for all the films with $h_0 = 0.4$–1.5 nm. We observe that $h(q_m)/h_0$ reaches unity with a small fraction of holes, i.e., dominant characteristic wavelengths are strongly correlated with initial rupture, only for $h_0 \leqslant 0.5$ nm. For $h_0 = 0.6$–1.0 nm, the growth of the dominant undulation wavelengths lags behind the formation of holes. Consequently, it would be incorrect to deduce that the characteristic wavelengths at t_m obtained from Fourier spectra are mere results of spinodal instability. For $h_0 = 1.2$–1.5 nm, there is no apparent characteristic surface undulation wavelength after $\approx$1.0 ns when the first holes appear [Fig. 3(c)]. The hole formation in these thick films is reminiscent of the description of thermal nucleation-induced dewetting.

We do not observe any hole form for $h_0 = 1.8$–2.0 nm after tens of nanoseconds with the substrate dimension up to $L \approx 460$ nm. To verify if these films are metastable, we remove the liquid atoms within a cylindrical patch of radius R and height h_0 from the film and examine if the resulting hole would spontaneously grow. For $h_0 = 2.0$ nm at $T = 1800$ K, patches with $R \geqslant 1.0$ nm would grow and those with $R < 1.0$ nm would collapse. For $R = 1.0$ nm, we vary the position of the patch and notice that the hole more likely expands than collapses. This finding is of practical importance for the present study because even if we were to increase L and to run simulations much longer, it is highly unlikely that the films of $h_0 \geqslant 2.0$ nm would dewet with the given temperature range and liquid density.

It is important to note the consistent fashion of the hole formation process for all values of h_0 studied, regardless of how strongly spinodal instability features correlate with initial rupture (see Fig. 4). This rupture behavior indicates the possibility of a unique driving force responsible for the rupture of these films at microscopic levels. Since the liquid atoms are equilibrated at constant temperature and volume, their dynamics is driven by free-energy minimization. In the following section, we correlate the system dynamics and the hole formation process from the liquid atoms' trajectories obtained by MD simulations.

C. Tendency to recover bulk-like local environment

From the continuum model perspective, the stability of the thin films of interest is characterized by the effective interfacial energy between the substrate-liquid and liquid-vapor interfaces [6,7,20]. In the particle-based model context, the interfacial energy is essentially the difference between the chemical potential of the thin film and that of the bulk liquid, both sandwiched by the substrate and vacuum at the given temperature [47–49]. Therefore, we investigate the energetic aspects of the rupture process with reference to the corresponding bulk liquid state. Similar to previous studies [49], we approximate the bulk liquid state as a thick film ($h_0 \approx 40.0$ nm) in contact with the substrate at the same temperature as the films of interest.

One natural measure for the film stability is the potential energy per liquid atom. The time evolution of the potential energy per liquid atom for different initial thicknesses is shown in Fig. 8(a). As h_0 increases, the per atom potential energy in the film before rupture gets closer to the bulk value; concurrently, the incubation time of U increases, corresponding to the increase in the rupture time. Upon rupture and subsequent dewetting, the potential energy, U, decreases toward the bulk liquid energy for all studied films. For all cases, U does not fully recover the bulk value because the resulting liquid droplets are kinetically trapped on the substrate surface and thus cannot coalesce into a single droplet to lower the energy further within the simulation time scale.

Another relevant metric to characterize both energetic and entropic aspects of the liquid atoms is their coordination number within a certain distance. Figure 8(b) shows the time evolution of the average coordination number of the liquid atoms, $C(r)$, within the distance of $r = 0.3$ nm in the films mentioned above. This distance is chosen to be slightly greater than the first peak of the pair correlation function of the liquid atoms in the bulk, i.e., at $r \approx 0.25$ nm. As can be seen, the coordination number correlates well with the per-atom energy, suggesting that the decrease in potential energy indeed results from the liquid atoms attempting to increase their coordination toward bulk values. The tendency both in per-atom potential energy and coordination number indicates that the thin films are energetically unstable compared to the bulk state and quantifies the enthalpic driving force for dewetting. As h_0 increases, however, the driving force for rupture decreases because the difference in the local environment of the liquid atoms in the film and in bulk becomes less pronounced.

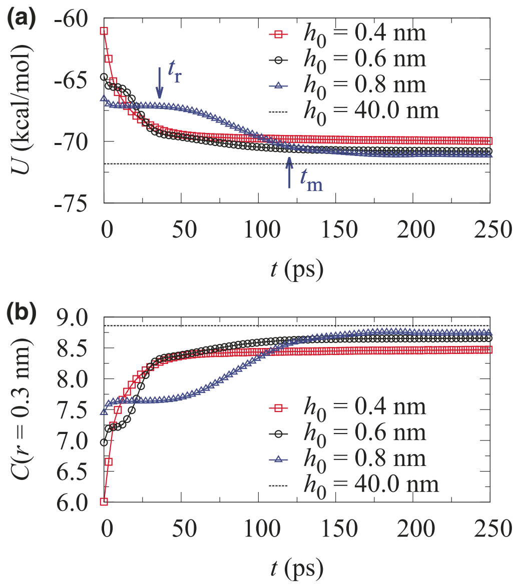

FIG. 8. (Color online) Time evolution of (a) potential energy per liquid atom and (b) average coordination number of liquid atoms for $L = 383$ nm at $T = 1800$ K.

IV. DISCUSSION

Our key results can be summarized as follows. We have shown that our coarse-grained model of the thin-film systems can produce results with excellent qualitative agreement with previous experimental studies with regards to dewetting pathways. By characterizing the spatial correlation of local thickness, we demonstrate that the features of spinodal instability and thermal nucleation coexist in the range of initial thickness under investigation. Importantly, the hole number density and area fraction follow consistent trends, reminiscent of a hole nucleation process, for all values of h_0 and temperature. The driving force for the hole nucleation process is then attributed to the tendency of the liquid atoms to recover their bulk-like local environment in the presence of thermal fluctuations exerted on individual atoms. Finally, we stress that care should be taken when interpreting dewetting patterns as mere consequences of spinodal instability from experimental data at the hole coarsening stage (i.e., $t \geqslant t_m$) and from simulation data with insufficiently large substrate dimensions.

Similar to liquid-crystal films [55], the metallic films in the present study are shown to dewet due to thermal fluctuations *within* the liquid volume. Several continuum models have taken into account the effects of thermal fluctuations inside the film, for example, in terms of thermoacoustic disjoining pressure [35–37], where it was shown that thermal fluctuations alone led to spinodal instability in certain cases. In our model, these effects are explicitly represented by the coupling between individual liquid atoms and the heat bath (i.e., the thermostat). From the energetic analysis in the previous section, we have shown that thermal fluctuations enable the liquid atoms to evolve toward more stable energetic configurations, which in turn are characteristic of spinodal instability and thermal nucleation seen from macroscopic scales. As a result, we argue that the two dewetting pathways, spinodal instability and thermal nucleation, from the continuum model perspective actually have the same origin at microscopic levels. It then follows that spinodal instability are characteristics of the hole formation process that become particularly pronounced for a certain range of initial film thickness and temperature. This view could help explain previous experimental observations that cannot be reconciled by the classical view of separate spinodal and nucleation regimes (e.g., spinodal-like surface undulations induced by thermal nucleation [24,63] or nucleation-induced dewetting within the linear unstable regime [15,25]). If we consider the free-energy barrier for hole nucleation a function of film thickness and temperature [25,26], the barrier increases as h_0 increases or as temperature decreases toward the liquid-solid transition temperature T_m. Thus, we can attribute the metastability of the films to the vanishing hole nucleation rate in the limit of $h_0 \to \infty$ and $T/T_m \to 1^+$.

It is necessary to address the primary difference between our simulation results and experimental data, which is the thickness threshold beyond which the films become metastable. We found this threshold to be approximately 2.0 nm, which is an order of magnitude smaller than in experiment. Because we couple individual liquid atoms with the heat bath using the Nose-Hoover thermostat, there is no temperature gradient in our simulations across the film thickness. Meanwhile, dewetting in metallic thin films on top of silicon oxide substrates is often induced by nanosecond laser irradiation. In those cases, experimental and theoretical studies have shown that laser irradiation leads to a temperature gradient, and hence a density gradient, across the film thickness [33,34]. The temperature gradient results in thermocapillary effects that could destabilize the films under certain conditions. It is possible to apply a temperature gradient in our model, e.g., by adding and removing atom kinetic energy at the top and bottom of the films, respectively. For example, Schebarchov *et al.* suggest regulating the liquid-film temperature through the solid substrate, of which the top layer contains mobile atoms whose dynamics is coupled with a thermostat [54]. We will consider this topic in future studies.

Along with our previous study [55], it becomes evident that thin-film dewetting is an excellent subject for large-scale molecular simulation in favor of the increasing capability of supercomputers. On one hand, molecular simulations allow us to closely examine the dewetting dynamics at early stages, from which a rigorous characterization of surface undulations and the hole formation process can be performed. On the other hand, only by approaching experimental scales are we able to have reliable interpretations of dewetting behaviors and of the relationship between dewetting patterns and initial thickness, which were inaccessible by previous studies using small system sizes. Using insufficiently large substrate dimensions leads to substantially longer rupture times and considerably fewer holes. The former could lead to the erroneous conclusions that the films were metastable and the latter gives rise to poor statistics on the hole formation rate and finite-size effects due to periodic boundary conditions.

V. CONCLUSION

The coexistence of spinodal instability and thermal nucleation is well known in polymeric and metallic thin films, which leads to various, sometimes controversial, interpretations on the rupture mechanism in certain cases. Using a minimal model and molecular simulation with length scales comparable to experimental systems, we have demonstrated that at molecular levels these two dewetting pathways originate from the tendency of the liquid atoms, initially confined in the thin film, to achieve more energetically favorable configurations. Depending on initial thickness and temperature, the hole nucleation process exhibits distinctive features of spinodal instability, via liquid retraction or hole expansion, simultaneously with the formation of spatially and temporally random holes induced by thermal fluctuations. Our study serves not only to provide new insights into the dewetting behavior of liquid films from molecular levels but also to inspire future systematic investigation on important factors such as liquid-substrate and liquid-liquid surface tensions, substrate morphology, application of external fields, and other nonequilibrium effects.

ACKNOWLEDGMENTS

The authors acknowledge helpful discussion with Lou Kondic, Javier Diez, and Alejandro G. González. T.D.N. thanks W. Michael Brown for technical support and helpful discussion. M.F.C. and J.D.F. acknowledge support from the Center for Nanophase Materials Sciences, which is sponsored at Oak Ridge National Laboratory by the Scientific User Facilities Division, Office of Basic Energy Sciences, US Department of Energy. P.D.R. acknowledges support from NSF Grant No. CBET-1235651. This research used resources of the Leadership Computing Facility at Oak Ridge National Laboratory and was conducted under the auspices of the Office of Advanced Scientific Computing Research, Office of Science, US Department of Energy, under Contract No. DE-AC05-00OR22725 with UT-Battelle, LLC. Accordingly, the US Government is authorized to reproduce and distribute reprints for Governmental purposes notwithstanding any copyright annotation thereon.

---

[1] M. A. Green, J. Mater. Sci.: Mater. Electron. **18**, S15 (2007).
[2] P. Innocenzi and L. Malfatti, Chem. Soc. Rev. **42**, 4198 (2013).
[3] A. Vrij, Discuss. Faraday Soc. **42**, 23 (1966).
[4] M. B. Williams and S. H. Davis, J. Colloid Interface Sci. **90**, 220 (1982).
[5] F. Brochard-Wyart and J. Daillant, Can. J. Phys. **68**, 1084 (1990).

[6] R. Khanna and A. Sharma, J. Colloid Interface Sci. **195**, 42 (1997).
[7] A. Sharma and R. Khanna, Phys. Rev. Lett. **81**, 3463 (1998).
[8] U. Thiele, M. G. Velarde, and K. Neuffer, Phys. Rev. Lett. **87**, 016104 (2001).
[9] J. A. Diez, A. G. González, and L. Kondic, Phys. Fluids **21**, 082105 (2009).
[10] J. Sarkar and A. Sharma, Langmuir **26**, 8464 (2010).
[11] N. Shirato, H. Krishna, and R. Kalyanaraman, J. Appl. Phys. **108**, 024313 (2010).
[12] J. N. Israelachvili, *Intermolecular and Surface Forces*, 3rd ed. (Academic Press, London, 2011).
[13] U. Thiele, Eur. Phys. J. E **12**, 409 (2003).
[14] G. Reiter, Eur. Phys. J. E **12**, 465 (2003).
[15] O. K. C. Tsui, Y. J. Wang, H. Zhao, and B. Du, Eur. Phys. J. E **12**, 417 (2003).
[16] H. Kaya and B. Jerome, Eur. Phys. J. E **12**, 383 (2003).
[17] J. Bischof, D. Scherer, S. Herminghaus, and P. Leiderer, Phys. Rev. Lett. **77**, 1536 (1996).
[18] R. Xie, A. Karim, J. F. Douglas, C. C. Han, and R. A. Weiss, Phys. Rev. Lett. **81**, 1251 (1998).
[19] R. Seemann, S. Herminghaus, and K. Jacobs, Phys. Rev. Lett. **86**, 5534 (2001).
[20] G. Reiter, A. Sharma, A. Casoli, M. David, R. Khanna, and P. Auroy, Langmuir **15**, 2551 (1999).
[21] G. Reiter, A. Sharma, and R. Khanna, Phys. Rev. Lett. **85**, 1432 (2000).
[22] S. Herminghaus, K. Jacobs, K. Mecke, J. Bischof, A. Fery, M. Ibn-Elhaj, and S. Schlagowski, Science **282**, 916 (1998).
[23] J. Becker, G. Grn, R. Seemann, H. Mantz, K. Jacobs, K. R. Mecke, and R. Blossey, Nat. Mat. **2**, 59 (2003).
[24] C. Bollinne, S. Cuenot, B. Nysten, and A. M. Jonas, Eur. Phys. J. E **12**, 389 (2003).
[25] Y. J. Wang and O. K. C. Tsui, Langmuir **22**, 1959 (2006).
[26] A. B. Croll and K. Dalnoki-Veress, Soft Matter **6**, 5547 (2010).
[27] H. Krishna, R. Sachan, J. Strader, C. Favazza, M. Khenner, and R. Kalyanaraman, Nanotechnology **21**, 155601 (2010).
[28] Y. Wu, J. D. Fowlkes, P. D. Rack, J. A. Diez, and L. Kondic, Langmuir **26**, 11972 (2010).
[29] S. Strobel, C. Kirkendall, J.-B. Chang, and K. K. Berggren, Nanotechnology **21**, 505301 (2010).
[30] Y. Wu, J. D. Fowlkes, N. A. Roberts, J. A. Diez, L. Kondic, A. G. González, and P. D. Rack, Langmuir **27**, 13314 (2011).
[31] J. D. Fowlkes, L. Kondic, J. A. Diez, Y. Wu, and P. D. Rack, Nano Lett. **11**, 2478 (2011).
[32] A. Sharma, J. Mittal, and R. Verma, Langmuir **18**, 10213 (2002).
[33] J. Trice, C. Favazza, D. Thomas, and R. Kalyanaraman, Phys. Rev. Lett. **101**, 017802 (2008).
[34] A. Atena and M. Khenner, Phys. Rev. B **80**, 075402 (2009).
[35] E. Schäffer and U. Steiner, Eur. Phys. J. E **8**, 347 (2002).
[36] M. D. Morariu, E. Schäffer, and U. Steiner, Eur. Phys. J. E **12**, 375 (2003).
[37] M. D. Morariu, E. Schäffer, and U. Steiner, Phys. Rev. Lett. **92**, 156102 (2004).
[38] K. Mecke and M. Rauscher, J. Phys.: Condens. Matter **17**, S3515 (2005).
[39] G. Grün, K. Mecke, and M. Rauscher, J. Stat. Phys. **122**, 1261 (2006).
[40] R. Fetzer, M. Rauscher, R. Seemann, K. Jacobs, and K. Mecke, Phys. Rev. Lett. **99**, 114503 (2007).
[41] P. Ziherl, R. Podgornik, and S. Zumer, Phys. Rev. Lett. **84**, 1228 (2000).
[42] J. De Coninck, S. Hoorelbeke, M. P. Valignat, and A. M. Cazabat, Phys. Rev. E **48**, 4549 (1993).
[43] A. Milchev and K. Binder, J. Chem. Phys. **106**, 1978 (1997).
[44] N. Akino, F. Schmid, and M. P. Allen, Phys. Rev. E **63**, 041706 (2001).
[45] V. P. Carey and A. P. Wemhoff, J. Heat Transfer **128**, 1276 (2006).
[46] E. Bertrand, T. D. Blake, V. Ledauphin, G. Ogonowski, and J. De Coninck, Langmuir **23**, 3774 (2007).
[47] D. Bhatt, J. Newman, and C. J. Radke, J. Phys. Chem. B **106**, 6529 (2002).
[48] D. Bhatt, J. Newman, and C. J. Radke, J. Phys. Chem. B **107**, 13076 (2003).
[49] M. Han, Colloids and Surfaces A: Physicochem. Eng. Aspects **317**, 679 (2008).
[50] A. M. Willis and J. B. Freund, Phys. Fluids **22**, 022002 (2010).
[51] N. Tretyakov, M. Müller, D. Todorova, and U. Thiele, J. Chem. Phys. **138**, 064905 (2013).
[52] T. D. Nguyen, M. Fuentes-Cabrera, J. D. Fowlkes, J. A. Diez, A. G. González, L. Kondic, and P. D. Rack, Langmuir **28**, 13960 (2012).
[53] J. Koplik and J. R. Banavar, Phys. Rev. Lett. **84**, 4401 (2000).
[54] D. Schebarchov, B. Lefèvre, W. R. C. Somerville, and S. C. Hendy, Nanoscale **5**, 1949 (2013).
[55] T. D. Nguyen, J.-M. Y. Carrillo, M. A. Matheson, and W. M. Brown, Nanoscale **6**, 3083 (2014).
[56] M. S. Daw and M. I. Baskes, Phys. Rev. B **29**, 6443 (1984).
[57] M. Foiles, M. I. Baskes, and M. S. Daw, Phys. Rev. B **33**, 7983 (1986).
[58] M. Fuentes-Cabrera, B. H. Rhodes, J. D. Fowlkes, A. López-Benzanilla, H. Terrones, M. L. Simpson, and P. D. Rack, Phys. Rev. E **83**, 041603 (2011).
[59] S. Plimpton, J. Comp. Phys. **117**, 1 (1995).
[60] W. M. Brown, P. Wang, S. J. Plimpton, and A. N. Tharrington, Comput. Phys. Commun. **182**, 898 (2011).
[61] W. M. Brown, T. D. Nguyen, M. Fuentes-Cabrera, J. D. Fowlkes, P. D. Rack, M. Berger, and A. S. Bland, Procedia Comput. Sci. **9**, 186 (2012).
[62] D. Frenkel and B. Smit, *Understanding Molecular Simulation: From Algorithms to Applications* (Academic Press, San Diego, 2002).
[63] T. Kerle, R. Yerushalmi-Rozen, J. Klein, and L. J. Fetters, Europhys. Lett. **44**, 484 (1998).
[64] M. Cieplak, J. Koplik, and J. R. Bavanar, Physica A **287**, 153 (2000).